Applications in Engineering Science 3 (2020) 100011

Contents lists available at ScienceDirect

Applications in Engineering Science

journal homepage: www.elsevier.com/locate/apples

A model for optimizing hooked end steel fibre reinforcements in cracked cement composites

C.A. Nonato Da Silva [a], J. Ciambella [a,*], J.A.O. Barros [b], I.G. Costa [c]

[a] Department of Structural and Geotechnical Engineering, Sapienza University of Rome, Italy
[b] Departamento de Engenharia Civil, University of Minho, ISISE, IB-S, Portugal
[c] Civitest - Pesquisa de Novos Materiais para a Engenharia Civil, Portugal

ARTICLE INFO

Keywords:
Hooked end steel fibres
SFRC
Cohesive interface
Multiscale modelling

ABSTRACT

The addition of metallic fibres in concrete is a widely used technique to increase its resistance to crack opening, energy absorption capacity, and durability. The properties of the resulting composite strongly depend on the geometry of the fibres, which usually dispose of an hooked end, as well as on the mechanical properties of both the fibre and the concrete. The optimization of the fibre reinforcement mechanisms can only be achieved by an approach that takes into account adequately these aspects. Therefore, in this work, a computational model incorporating the key features of a hooked end fibre embedded in a cement matrix is proposed. The fibre is modelled as a Timoshenko beam, whereas a cohesive interface is used to model the interaction with the surrounding concrete. Different failure mechanisms are defined including fibre debonding or fibre tensile rupture and concrete spalling at fibre exit point. The model is calibrated by using the results of an experimental campaign conducted by authors. A multi-step optimization algorithm is used to find the optimal geometry and model's constitutive parameters that maximize the peak pull-out force and the energy absorption capacity in a fibre pull-out test. The analysis suggests that the use of concrete with high strength has the potential to increase both peak force and energy absorption capacity by designing the proper geometry of the fibre.

1. Introduction

A large number of research studies on Fibre Reinforced Concrete (FRC) has been devoted to assess the reinforcement potentialities of discrete fibres (Alwan et al., 1999; Robins et al., 2002; Song, 2012; Zīle and Zīle, 2013). One of the reasons is their ability to control the crack opening and propagation by bridging the crack faces and providing resistance to crack opening whichever directions the cracks form (Cunha et al., 2010). This mechanism starts at microlevel, since the addition of fibres offers resistance to micro-cracks to degenerate in meso- and macro-cracks delaying their propagation and favour the development of multiple smaller cracks (Isla et al., 2015; Lancioni and Alessi, 2020). These characteristics become particularly attractive in demanding environments, such as tunnel linings and maritime applications, where hybrid reinforcements (fibres and conventional steel bars or grids) can provide a significant increase in the system performance. If resisting mechanisms of fibres crossing the cracks are capable of supporting the applied external forces, fibres can replace or eliminate the use of conventional reinforcements with significant economic benefits (Khabaz, 2016). Among the different type of fibres available in the market, hooked end steel fibres are the most used for structural applications because their anchorage mechanisms, together with their length and tensile strength, offers additional additional pull-out resistance and may further improve the performance of the structural element, compared to smooth fibre. In any case, the rheology of the steel fibre reinforced concrete (SFRC), the casting conditions and the geometry of the structural member to be produced must be also considered in the modelling due to their significant impact on the fibre distribution and orientation profile (Abrishambaf et al., 2015). The peak pull-out resisting force of hooked end type fibres can be attained for a crack width do not exceeding the limits imposed by the serviceability limit state design conditions, as long as the geometry and properties of the materials are properly evaluated, which can have significant technical and economics benefits in the civil construction industry (Laranjeira et al., 2010).

The hooked end contribution to the pull-out mechanism depends mainly on the fibre tensile strength, fibre orientation, the hook geometry and the strength of the surrounding cement-based matrix (Cunha et al., 2010). The accurate description of the reinforcement mechanisms provided by the hook is crucial for designing the fibre and optimising the effectiveness of the reinforcement system. To better understating these reinforcement mechanisms, many researchers have performed pull-out tests of a single hooked end fibre (Isla et al., 2015; Khabaz, 2016) and

* Corresponding author.
E-mail address: jacopo.ciambella@uniroma1.it (J. Ciambella).

https://doi.org/10.1016/j.apples.2020.100011
Received 30 June 2020; Received in revised form 3 August 2020; Accepted 11 August 2020
Available online 22 August 2020

have proposed analytical formulations for modelling the bond behaviour (Alessi et al., 2017; Cunha et al., 2010; Fantilli and Vallini, 2007; Laranjeira et al., 2010; Mazaheripour et al., 2016; Soetens et al., 2013; Zhan and Meschke, 2014). In all these contributions, the pull-out on hooked end fibres was modelled with a certain inclination of the fibre towards the applied load for capturing the relative orientation between the crack plane and the fibre. In Cunha et al. (2010) for instance, the contribution of the hooked end was modelled by adding an elastic spring at the end of a smooth fibre, where the stiffness of the spring was calibrated with the available experimental. The authors of Zhan and Meschke (2014) and Laranjeira et al. (2010) used a similar approach to incorporate the effects of the hook in their model. They considered a series of key states during the pull-out of the fibre and, for every key state, the additional pull-out force provided by the hook was calculated and added as an external force into a model of a straight fibre. Their formulation took into account several aspects of the response: the transverse force at the fibre exit point, the plasticity of the fibre, the concrete deformabilty and the matrix damage. In Zile and Zile (2013), a model was developed to simulate the hooked end by adding the friction between the fibre and the matrix during the pull-out and the plastic work required to straighten the fibre. The latter was found to be a function of geometric parameters and of the yield stress of the fibre.

In these previous works, the different mechanisms affecting the peak pull-out force and failure modes of aligned and inclined fibres were presented. The additional effects caused by the shear force and the bending moment on the fibre's cross section, mainly at its exit point (at crack section) have a significant impact on the peak force and they are determinant to lead the system to fail, which can either be by the complete debonding of the fibre, matrix spalling or the tensile rupture of the fibre. The spalling mechanism of the matrix at the fibre exit point, which was observed for a hook end fibre with a certain orientation, was taken into account in a model recently proposed in Nonato Da Silva et al. (2019) for smooth fibres. Indeed, the orientation is one of the mainly parameters to achieve the full potential of the pull-out system and the experiments carried out in Cunha et al. (2010) confirm that the force necessary to completely pull-out the fibre from the matrix increases with the inclination angle, if the fibre rupture does not occur. In addition, Nonato Da Silva et al. (2019) reported that up to a certain inclination, the work required to completely remove the inclined fibre from a cement matrix is higher than the one of an aligned fibre. Several investigations revealed similar tendencies and certified the existence of an optimal configuration in the terms of peak force and energy absorption capacity (Cunha et al., 2010; Laranjeira et al., 2010; Nonato Da Silva et al., 2019).

In this paper, the existence of optimal configurations of a fibre-matrix system tested in Tarifa et al. (2020) is thoroughly investigated. The analysis is carried out by adapting a microstructural model recently proposed by the authors (Nonato Da Silva et al., 2019) for smooth fibres. This model can account for an arbitrary orientation of the fibre toward the crack plane, for multiple branches of the fibre to simulate the hooked end or more complex geometric configurations. In addition, the model simultaneously accounts for all the relevant effects registered in the pull-out response, which are mostly neglected in the available literature contributions, including: fibre bending, matrix damage and matrix spalling. The fibre reinforcement is described through a one-dimensional model, which is used to solve the set of differential equations that governs the pull-out behaviour by considering the variation of the axial and transverse displacements, the axial and shear forces, and the bending moment along the fibre length. The fibre-matrix interaction is simulated through a cohesive-like interface, which allows the main experimental failure modes to be recovered, including fibre debonding and rupture, and matrix spalling. Experimental tests carried out in Tarifa et al. (2020) are used to assess the predicting capabilities of the model. Finally, a parametric analysis is conducted to find the optimal geometries that can maximise both the peak pull-out force and the energy absorption capacity.

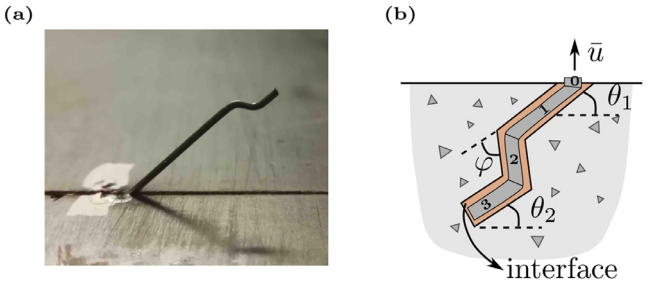

Fig. 1. (a) Picture of the real specimen used in Tarifa et al. (2020). (b) Schematic representation of the specimen with the different fibre segments used for modelling.

2. Model description

In this section, the model initially proposed for smooth fibres in Nonato Da Silva et al. (2019) is adapted for being possible the development of hooked end steel fibres of optimum reinforcement performance. The geometry of the system along with a picture of the real specimen are displayed in Fig. 1. The fibre consists of four segments, each one with a relative inclination with respect to the other. The segment 0, of fixed length $L_0 = 1$ mm, is used to model the real experimental setup in which the fibre is vertically pulled out by the testing machine. The angle that the fibre forms with the crack plane is indicated with θ_1, whilst the total length of the fibre is $L_b = L_0 + L_1 + L_2 + L_3$. Each segment of the fibre is modelled as a Timoshenko beam, thus the balance of axial N and shear T forces and bending moment M at each material point x gives

$$N'(x) - p\,\tau(x) = 0, \qquad M'(x) - T(x) = 0, \qquad T'(x) - q(x) = 0\,. \tag{1}$$

Here τ is the shear force transferred to the fibre by the cohesive interface and p is the perimeter of the fibre, whereas q is used to account for the reaction force of the cement matrix surrounding the fibre. In writing down Eq. (1), it is implicitly assumed that the interface has a vanishing thickness and can only transfer shear forces.

For each of the components of this FRC composite, the constitutive laws depicted in Fig. 2 are assumed: the metallic fibre has an elastic-brittle behaviour, typical of steel with high carbon content as the one used in the experiments; the interface has the cohesive-like response given by

$$\tau(u) = \begin{cases} \tau_m \frac{u}{u_I}\,, & u \le u_I \\ \tau_m\,, & u_I < u \le u_{II} \\ \tau_r + (\tau_m - \tau_r)\frac{u_{II}}{u}\,, & u > u_{II} \end{cases} \tag{2}$$

in which τ_m and τ_m/u_I are the bond strength and the elastic modulus of the interface, respectively, u_I is the sliding at the attainment of the bond strength and u_{II} is the sliding at which the bond stress capacity enters in a softening stage with an asymptotic evolution up to a residual value of τ_r. The τ_r is used to account for the friction force exerted when the fibre is completely debonded and can slide into the concrete channel. In Tarifa et al. (2020), it was observed that the peak pull-out force decreases with the increase of the fibre inclination angle; this behaviour is the manifestation of the complex micro-cracking mechanisms that happen in proximity of the fibre exit point and are the main responsible for a portion of the matrix being expunged, a phenomenon often referred to as *matrix spalling* (Zhan and Meschke, 2014). To account for this important effect, it was proposed in Nonato Da Silva et al. (2019) to make the parameter u_I of the bond-stress constitutive law dependent on the angle θ_1 (Fig. 1) by the relationships $u_I = u_I^0 \exp(\delta\,\theta_1)$, where δ is used to adjust the dependence of the sliding u_I with the fibre angle θ_1, and u_I^0 is the displacement for $\theta_1 = 0°$. As a consequence, the stiffness of the first branch of the bond interface law decreases with the increase of θ_1; this simple strategy allows these complex micro-mechanisms to be simulated. For what concerns the concrete, the following nonlinear

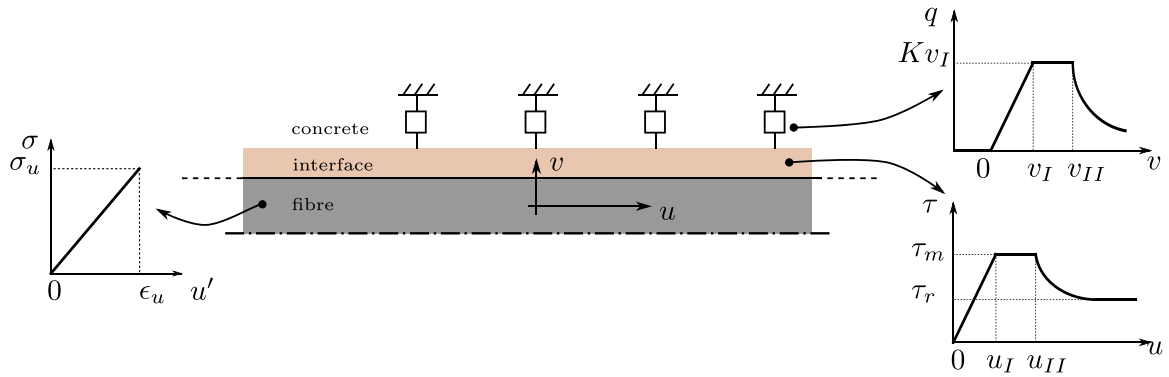

Fig. 2. Constitutive laws for the three components of the fibre reinforced concrete, where just half of the system is shown due to the symmetry with respect to the dot-dashed line.

foundation model with a cohesive-like behaviour is assumed:

$$q(v) = \begin{cases} Kv\,, & 0 < v \le v_I \\ Kv_I\,, & v_I < v \le v_{II} \\ Kv_I\,\frac{v_{II}}{v} & v > v_{II} \end{cases} \tag{3}$$

where K is the elastic stiffness of the concrete, v is the transverse displacement of the fibre, v_I represents the displacement at the attainment of the contact compressive strength and, finally, v_{II} is the displacement at which crushing starts being so significant that the fibre's supporting capacity decreases with the increase of the transverse deformation. Differently from the constitutive law of the interface, the concrete has a non-symmetric transverse deformation constitutive response, not being able to transfer tractions.

By using the compatibility equations for the Timoshenko beam (see Krenk and Høgsberg, 2013) together with the constitutive equations, one arrives at the following set of differential equation governing the elastic equilibrium:

$$\begin{cases} EI\,\vartheta_i''(x) - \kappa\,\vartheta_i(x) + \kappa\,v_i'(x) = 0 \\ \kappa\,v_i''(x) + q(v_i(x)) - \kappa\,\vartheta_i'(x) = 0 \\ EA\,u_i''(x) - p\,\tau(u_i(x)) = 0 \end{cases} \tag{4}$$

in which $\vartheta_i(x)$ is the rotation of the cross-section at position x and the subscript $i = 1, 2, 3$ indicates the fibre segments represented in Fig. 2. E is the elastic modulus of the fibre, A its cross-section area, and $\kappa = \eta AG$, $G = E/(2+2\nu)$ is the transverse modulus of elasticity of the material ($\nu = 0.3$ for the considered materials), in which η is the so-called Timoshenko shear coefficient (6/7 for fibres of circular cross section).

The use of the Timoshenko beam model to describe behaviour of a fibre resting on a pseudo-soil (concrete matrix) was proven to be effective in Nonato Da Silva et al. (2019), particularly for those FRC composites in which the diameter of the fibre is comparable with the length of a fibre segment. The solution of the system (4) has to be carried out numerically once the proper boundary conditions are enforced; for the fibre represented in Fig. 1, continuity of horizontal and vertical displacements, as well as equilibrium of forces and bending moment are imposed at the points where consecutive segments are connected. At the fibre exit point, displacement with null rotations is imposed, whereas null horizontal force and null bending moment are prescribed at the fibre end.

2.1. Model implementation

The system of nonlinear differential Eq. (4) was implemented in Matlab and solved through the built-in *ode45* function. The solution algorithm is schematically depicted in Fig. 3. A sensitivity analysis in terms of the parameters of the model and the geometry of the fibre was carried out in Nonato Da Silva et al. (2019) to assess the convergence of the solution for different discretization meshes. The main failure conditions observed in the experiments are accounted for by the model, namely fibre rupture, matrix spalling and fibre debonding. The spalling of the matrix is always coupled with debonding or rupture of the fibre and takes place before the total fibre debonding or reinforcement rupture occur, as experimentally observed in Cunha et al. (2010); Robins et al. (2002). Therefore, four failure modes are contemplated: fibre rupture with or without matrix spalling and debonding with or without matrix spalling. The fibre rupture is verified when $N/N_u + M/M_u + T/T_u = 1$, which represents the failure condition of a fibre subjected to normal and shear forces and bending moment. For a fibre with circular cross-section is given by, $N_u = \sigma_u A$, $T_u = \sigma_u A/\sqrt{3}$, and $M_u = 4\sigma_u r^3/3$, where σ_u is the ultimate strength of the fibre material and r is the fibre radius. This failure criterion was successfully applied in the model developed by the authors in Zhan and Meschke (2014), and is indicated to fibres with a limited plastic plateau, such as the metallic fibre with high carbon content used in the experiments considered in this work. In addition, matrix spalling was set to occur when the transverse force acting on the matrix near the fibre exit point T_{exit} is higher than a threshold value R_{sp}, which depends on the fracture toughness of the concrete and on the geometry of the fibre and was calculated in Nonato Da Silva et al. (2019) according to fracture mechanics criteria. In the region, where the spalling occur, the fibre is let unbounded and its actual length reduced in the numerical code. Finally, the complete debonding of the fibre was achieved when the entire interface was in its softening or plastic stage.

The initial calibration of the model was carried out by fitting the experimental results shown in Fig. 4. The hooked-end fibre had a diameter 0.75 mm and was embedded into a self-compacting concrete of 86 MPa compressive strength. The embedment length of $L_b = 22$ mm and three inclination values of the angle θ_1, 0, 30 and 60 degrees, were tested; for

```
1  Initialisation:
       ū = 0.1 mm, material parameters ( ... );
       s = 0, %SPALLING flag initialized to 0;
2  while ū < ū_max do
3      Solve Eq. (4);
4      Compute N, T, M;
5      if T_exit ≥ R_sp then
           %MATRIX SPALLING has occurred;
           %L_0 is unbounded and the model's geometry updated;
6          s=1;      %Spalling flag set to 1;
7      if N/N_u + T/T_u + M/M_u ≥ 1 then
8          Break();
           % FIBRE RUPTURE either with (s=1) or without (s=0) MATRIX
             SPALLING;
9      ū = ū + 0.1 mm
   %FIBRE DEBONDING either with (s=1) or without (s=0) MATRIX SPALLING ;
```

Fig. 3. The failure-mode prediction algorithm implemented in Matlab to solve Eq. (4).

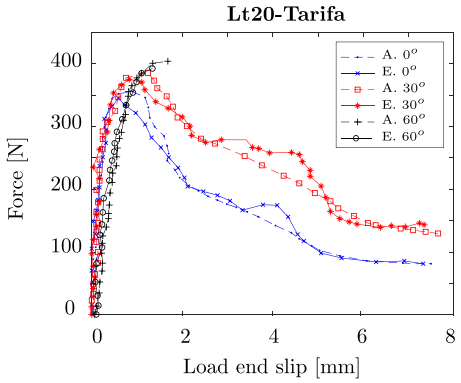

Fig. 4. Force vs displacement obtained by fitting the analytical model to the experimental data from (Tarifa et al., 2020) with $L_b = 22$ mm (A.=Analytical; E.=Experimental).

all fibre the internal angle φ was 41 degrees. The constitutive parameters of the fibre $E = 200$ GPa and $\sigma_u = 1.225$ GPa were obtained from the fibre datasheet provided by the manufacturer. The other parameters of the model $\mathfrak{p} = \{\tau_m, u_I, u_{II}, \delta, K, v_I, v_{II}\}$ were obtained by simultaneously fitting the data for the three angles in Fig. 4 through a nonlinear optimization algorithm in Matlab. The objective function was defined to minimize for all angles the difference between the numerical values of the force at the loaded end slip f and the corresponding values obtained from the experiments, $\hat{\mathbf{f}}$, that is

$$\min_{\mathfrak{p}} \sum_{\theta_1=\{0°,30°,60°\}} |\mathbf{f} - \hat{\mathbf{f}}|^2_{\theta_1} . \tag{5}$$

Due to the nonlinear nature of the governing equations, special procedure was adopted in solving (5) in order to avoid becoming trapped in local minima. In this procedure, the elastic modulus and tensile strength of fibre were kept fixed and the stability of the optimal solution was assessed by running the optimization algorithm multiple times with different values of the initial parameters and verifying after each iteration that the algorithm had converged to the same solution. For the data shown in Fig. 4, the optimal values of the constitutive parameters are:

$$\begin{aligned} &\tau_m = 2.10\,\text{MPa}\,, \quad \tau_r = 1.05\,\text{MPa}\,, \quad u_I^0 = 0.25\,\text{mm}\,, \quad \delta = 1.5 \\ &u_{II} = 1.3u_I\,, \quad K = 20\,\text{GPa}\,, \quad v_I = 0.20\,\text{mm}\,, \quad v_{II} = 0.22\,\text{mm} \end{aligned} \tag{6}$$

The results in Fig. 4 show the high accuracy in the fitting of both peak force and loaded-end slip for all fibre orientations and fibre embedment lengths. The pull-out response is made up of three parts, a feature common to all the experimental data considered. The fibres with 0° and 30° inclination shown similar pre-peak behaviour, however the nonlinear part is more pronounced in the 30°, due to the cracking and spalling of the matrix at the fibre bending point, as a consequence of the additional stress concentration in this zone. However, for the fibre oriented at the highest inclination (60°), the decay in the force for low end slip represents the pressure introduced by the fibre in the matrix at the exit point region which leads to matrix spalling, and consequently, a decrease in stiffness is observed. During this spalling process, the fibre in this region has moved in order to be aligned with the loading direction, and as a consequence a higher shear force and the bending moment is observed when compared with lower angles (see Fig. 8); this in turn leads to the tensile rupture of the fibre at lower loaded end slip compared to the other fibre orientations. For both 30° and 60° specimen, the post-peak behaviour shows a similar trend where the decrease of pull-out with the increase of loaded end slip is mainly governed by the frictional resistance of the surrounding matrix. This softening stage is also well captured by the model.

1 **Initialisation**:
  Set $\{L_b^{(i)}, \theta_1^{(i)}, \theta_2^{(i)}, \varphi^{(i)}, L_1^{(i)}/L_2^{(i)}, L_3^{(i)}/L_2^{(i)}, \sigma_u^{(i)}, f_{cm}^{(i)}\}$ from [17];
2 **Optimize** L_b and θ_1;
3 **Optimize** L_1/L_2, L_3/L_2 ;
4 **Optimize** θ_2 and φ;
5 **Optimize** σ_u and f_{cm};
  OPTIMAL SET
  $\{L_b^{(opt)}, \theta_1^{(opt)}, \theta_2^{(opt)}, \varphi^{(opt)}, L_1^{(opt)}/L_2^{(opt)}, L_3^{(opt)}/L_2^{(opt)}, \sigma_u^{(opt)}, f_{cm}^{(opt)}\}$;

Fig. 5. Optimization strategy used to get the optimal values of the geometric and material parameters of the FRC composite.

3. Optimization of the hooked end fibre/matrix system

The analytical model detailed in previous section is here applied to the optimisation of the geometry and material properties of the matrix fibre system. The material properties extracted by fitting the experimental data in Fig. 4 are listed in Eq. (6); among the geometric parameters, L_b, θ_1, θ_2, φ, L_1/L_2 and L_3/L_2 were selected to evaluate their influence on peak force, energy absorption capacity and failure mode. Afterwards, the influence of concrete compressive strength and fibre tensile strength (f_{cm}, σ_u) is assessed, since preliminary studies have shown that these parameters greatly affect the fibre pull-out response. In particular, due to the highly nonlinear character of the proposed model, a multi-step optimization procedure was followed. First, the influence on the peak force and energy absorption capacity of the fibre embedment length and inclination angle were investigated; thereafter, starting from the optimal configuration achieved, the effects of the internal lengths and, successively, of the internal angles were appraised. The schematic description of this algorithm is shown in Fig. 5. To obtain conclusions as a broad application as possible, the results at each step are presented in terms of peak force and energy dissipation capacity normalised with respect to the optimal configuration achieved at the previous step; in such a way, direct indication of the enhancement provided by the parameter being optimised is obtained. In all plots, the energy was obtained by calculating the area under the pull-out force versus load end slip relationship.

3.1. *Effect of embedment length* (L_b) *and fibre inclination* (θ_1)

First, the influence of the fibre embedment length L_b in its pull-out force, energy absorption and failure mode is evaluated. The analysis was carried out by fixing the geometry of the hook, according to the values provided in Eq. (6).

Fig. 6 a shows that by increasing the fibre inclination its tensile rupture occurs for smaller normalized peak force. Above an angle θ_1 of about 40 degrees, fibre tensile rupture is the failure mode even for embedment length of 10 mm. Fig. 6b shows that energy absorption is always higher if fibre debonding is the failure mode rather than fibre tensile rupture. The maximum energy absorption occurs in the intervals 15 to 25 degrees for θ_1 and 20 to 35 mm for L_b. By increasing the fibre inclination towards the fracture surface (θ_1), the shear stresses and bending moments in the fibre exit point region increases by affecting detrimentally the fibre tensile strength, causing the premature tensile rupture of the fibre, as demonstrated in Robins et al. (2002), Cunha et al. (2010) and Laranjeira et al. (2010). Inclined fibre mobilizes extra resisting mechanisms compared to aligned fibre, and as long as the fibre does not fail by tensile rupture, the maximum pull-out force increases with the fibre inclination.

The failure mode map for the hooked end fibre-matrix system is shown in Fig. 7. This plot gives an overview of the different failure mechanisms that occur for different geometric configurations of the fibre, as well as of the changes of the peak force value. When the inclination angle increases, the peak force has a maximum at relatively low embedment lengths and then it remains constant, meaning that in SFRC where fibres have a tendency to cross the cracks with a relatively high angle, and consequently to develop concrete spalling at the exit point of the fibre, no benefits in terms of fibre reinforcement are obtained by

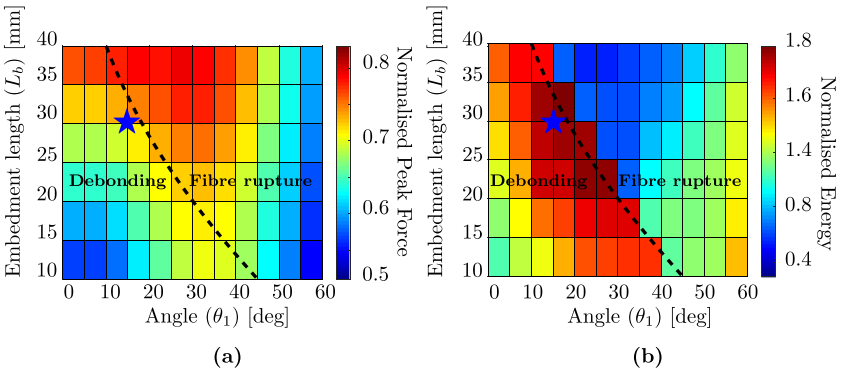

Fig. 6. Contour plot of the peak pull-out force (a) and energy absorption capacity (b) for $\theta_1 \in [0, 60]$ and $L_b \in [10, 40]$ mm. The thick dashed lines show the transition between two failure modes given by Eq. (8): complete debonding of the fibre from the matrix or fibre rupture. The blue star indicates the optimal configuration chosen to carry out the sensitivity analysis in Section 3.2.

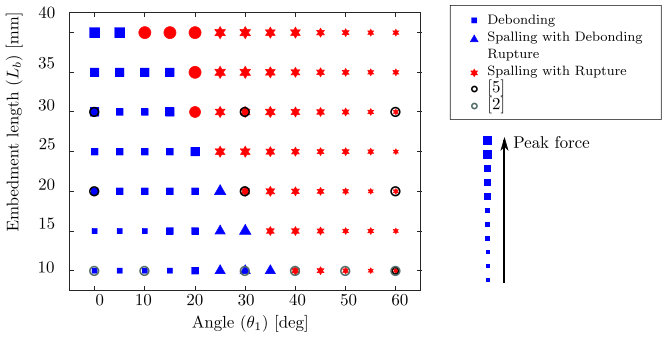

Fig. 7. Failure mode map in the θ_1 and L_b space for the SFC from Tarifa et al. (2020). The black and grey circles shows the data from Cunha et al. (2010) and Robins et al. (2002) where similar configurations were tested.

using longer fibres. Using smaller fibres (and consequently with smaller embedment length) but with the same volume fraction has more probability of providing higher reinforcement efficiency (higher number of fibres bridging the crack if the diameter is the same or even smaller), and this can also be seen by the size of the dots in Fig. 7, indicating the peak force value remains almost constant for angles between 25° and 40°*irc*; above 40° fibres fail by tension. The transition between debonding and fibre rupture can be approximated by the following dimensionless second order equation:

$$\frac{L_b}{L_f} = 0.61\theta_1^2 - 1.44\theta_1 + 0.89, \tag{7}$$

represented in Fig. 6 by dashed lines. Due to the high R-square value ($R^2 = 0.985$) of a linear equation, the term θ_1^2 can be neglected for design simplifications leading to

$$\frac{L_b}{L_f} = -1.02\theta_1 + 0.85, \tag{8}$$

where θ_1 is expressed in radians. Fig. 6b evidences that the normalised energy has an abrupt decay in the region just right of the limit defined by Eq. (7). Given that fibre rupture is an undesirable failure mode, due to the loss of fibre reinforcement mechanisms, pull-out model can then be used to provide some valuable insights and optimise the design of concrete reinforced with hooked end steel fibres, as will be presented in the following pages.

The pull-out resistance provided by the hook is evidenced in Fig. 8 where the internal actions (normal and shear forces, and bending moment) are compared for two inclination angles, $\theta_1 = 15°$ and $\theta_1 = 60°$, with fixed embedment length $L_b = 30$ mm. At the lower angle, the anchorage effect is provided mainly by the hook and in fact the internal stresses are higher in the hook region, corresponding to the curvilinear abscissa ξ_2 and ξ_3 in the figure. On the other hand, when the inclination towards the crack plane increases, there is a stress accumulation between segment 0 and 1, that in turn may lead to matrix spalling and eventually to fibre rupture.

One of the main reasons to add discrete fibres into concrete is to prevent crack propagation and limit the crack opening in-service lifetime. The maximum admissible crack width in normal operative condition is between 0.1 to 0.3 mm (Soudki and Alkhrdaji, 2004). In reinforced concrete structures, crack width at the level of a certain reinforcement is between one to two times the sliding ($\bar{u}$) of this reinforcement. Therefore, the optimisation of the hooked end fibres should assure the maximum pull-out force for a loaded end slip varying between 0.05 mm and 0.15 mm. Analysing the results from Fig. 6, it is seen that at angles of $\theta_1 = 15^o - 25^o$ and bond length of $L_b = 20 - 30$ mm, both peak force and energy absorption are maximised without rupture of the fibre.

It is further pointed out that the maximum embedment length L_b was restricted to 30 mm, because the hooked ends fibres available in the market have a total length L_f that varies between 30 and 60 mm and considering the fact that L_b in SFRC can be statistically estimated as $L_f/4$ (see Wang, 1989) with a maximum of $L_f/2$ (symmetry). Therefore, in the rest of this section, a configuration with $\theta_1 = 15^o$ and $L_b = 30$ mm was chosen to be optimized as as it has the potentiality to achieve high performance in term of peak force and energy absorption capacity.

3.2. *Effect of the fibre embedment parts* (L_1, L_2 *and* L_3)

To find the optimal relationship between the lengths (L_1, L_2 and L_3), the embedment length ($L_b = 30$ mm) and the angles ($\theta_2 = \varphi = 45°$ and $\theta_1 = 15°$) were kept fixed for the analysis in this section.

Fig. 9 shows the normalised peak pull-out and the normalised energy absorption capacity for different values of the ratios L_1/L_2 and L_3/L_2. The normalisation was carried out with respect to the optimal configuration in Fig. 6, indicated with a star, which corresponded to $L_1/L_2 = 9.8$ and $L_3/L_2 = 0.88$. By varying the L_1/L_2 ratio, the peak pull-out force can be increased by 10% if L_1/L_2 is set between 1 and 3, which corresponds to a significant reduction compared to the initial ratio $L_1/L_2 = 9.88$. For ratios $L_/L_2$ higher than 3, the effect on the peak force is indeed detrimental. In terms of L_3/L_2, the maximum force is achieved when $L_3/_2 = 1.2$, which is close to the initial values of 0.88.

Regarding the energy absorption capacity (Fig. 9b), it is seen that the energy had a behaviour similar to the peak force, since for all the configurations analysed the composite failed by fibre debonding. The results show that the higher performance of the hooked end fibres is mainly due to the mobilisation of the hook and its straightening. In fact for the interval considered for L_1/L_2, the normalized force has varied between 0.85 (minimum value) and 1.07 (maximum value). In terms of normalized energy this interval was a little bit higher (0.65 to 1.15), so the effect of the hook end seems to have a higher impact on the peak pull-out force than in the energy absorption capacity.

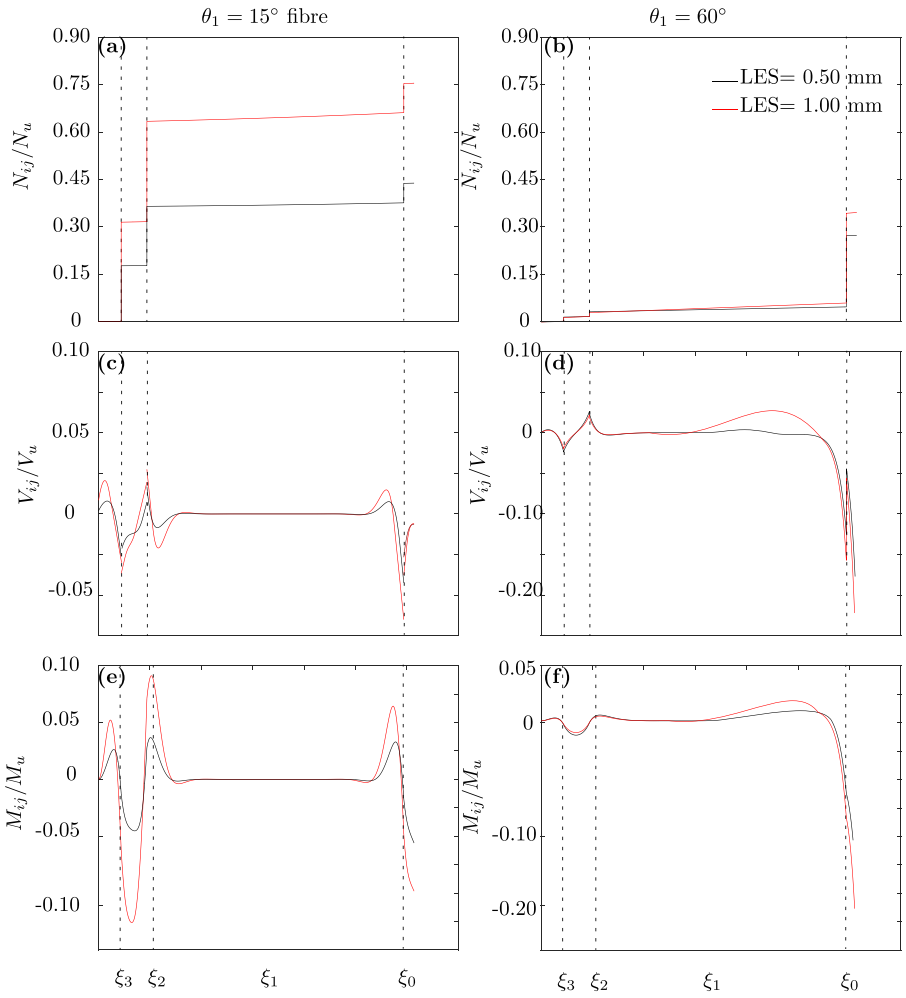

Fig. 8. Normalised axial and shear forces and bending moment along the fibre length for a fibre with $\theta_1 = 15^o$ (a,c,e) and $\theta_1 = 60°$ (b,d,f), where LES is the load end slip. ξ_i represents the curvilinear abscissa along each fibre segment.

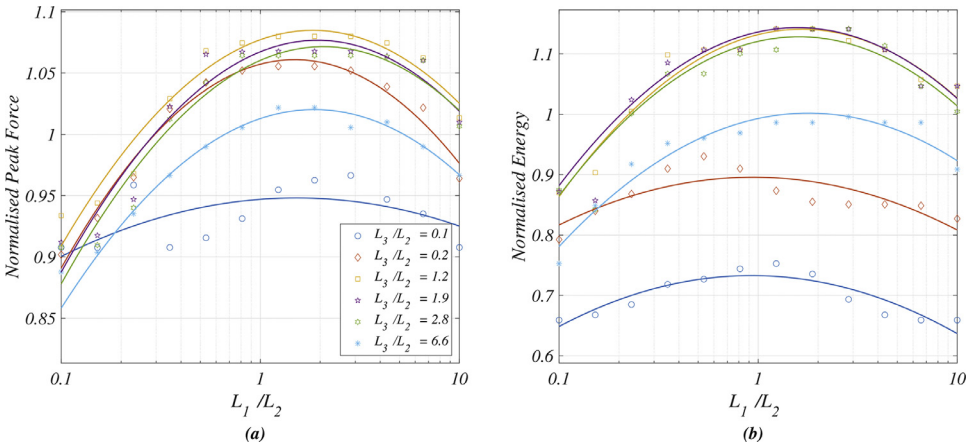

Fig. 9. Peak pull-out force (a) and energy absorption capacity (b) in terms of $L_1/L_2 \in [0.1, 10]$ and $L_3/L_2 \in [0.1, 6.66]$. The peak force and the energy are normalised with respect to the optimal configuration in Fig. 6, which was achieved for $L_1/L_2 = 9.8$ and $L_3/L_2 = 0.88$.

3.3. Effect of internal angles (θ_2 and φ)

The influence of the internal angles (θ_2 and φ) on the peak force and energy absorption capacity, is evaluated for a configuration with $\theta_1 = 15^o$ and $L_b = 30$ mm, for which the highest performance in terms of peak force and energy absorption capacity was obtained (see Fig. 6b). The optimal configuration of these internal angles was found to be $\varphi = 45^o$ with $\theta_2 = 55^o$, as Fig. 10a shows. The results demonstrated that internal angles in the range of 40^o to 55^o, increase the resistance to straighten and pull-out the fibre, and, consequently, the peak pull-out load increases. For higher angles ($> 55^o$), the stress concentration in the curvature regions decreases the local tensile strength of the steel. This was assessed experimentally and considered in some models from the literature, such is the case described by Barros and Foster (2018), where the tensile strength (designated as effective tensile strength by the authors) decreases with the inclination of the fibre. Despite the present model does not capture this effect directly, it is indirectly considered through stopping condition for the fibre rupture since the higher generalized forces in the transition zones can anticipate the tensile rupture of the fibre. Regarding the optimal values of both peak force and en-

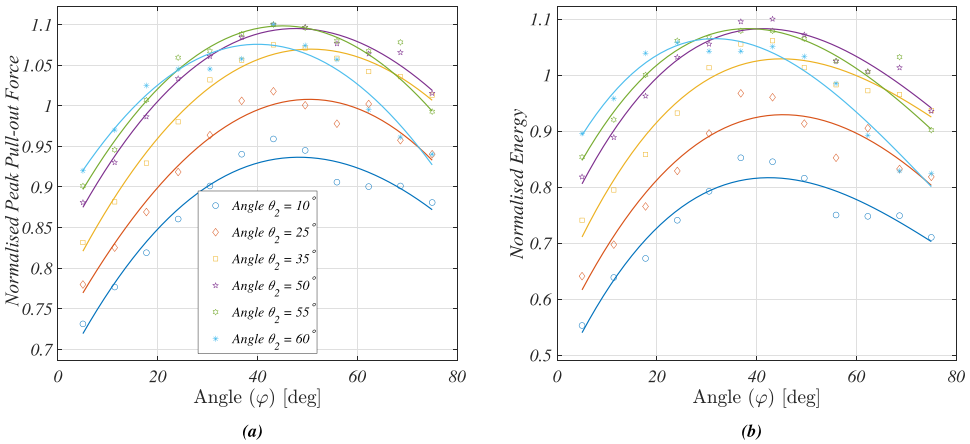

Fig. 10. Peak pull-out force (left) and energy absorption capacity (right) for $\varphi \in [15^{\circ}, 75^{\circ}]$ and $\theta_2 \in [15^{\circ}, 75^{\circ}]$. The peak force and the energy were normalised with respect to the optimal configuration in Fig. 6 that corresponded to $\varphi = 42^{\circ}$ and $\theta_2 = 41^{\circ}$.

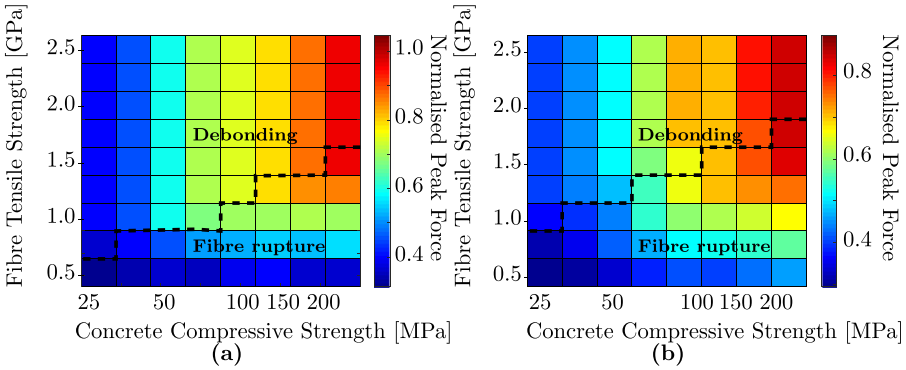

Fig. 11. Contour plot of the normalised peak force for fibre oriented at 15^{o} (a) and 60^{o} (b), for a concrete strength in the range [25,200] MPa and fibre tensile strength in [0.5,2.5] GPa. The normalisation is carried out for a fibre with $P_{fu} = \sigma_u A$ equal to 530 N.

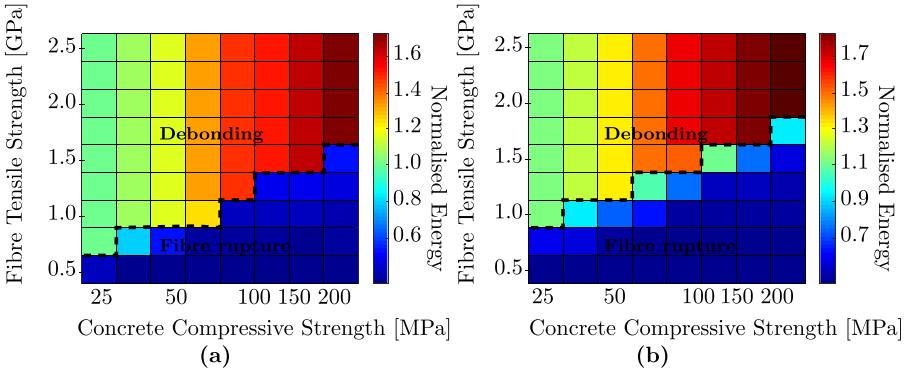

Fig. 12. Contour plot of the normalised energy for fibres oriented at 15^{o} (a) and 60^{o} (b) fibres for a concrete strength in the range [25,200] MPa and fibre tensile strength in [0.5,2.5] GPa. The thick dashed lines show the transition between two failure modes: complete debonding of the fibre from the matrix or fibre tensile rupture.

ergy, the interval was found to be $35 < \varphi < 50$ and $45 < \theta_2 < 65$, which roughly corresponded to an increase of 10% in the peak force and 5% of the energy absorption capacity. In addition, debonding was the observed failure mode independently of the angles θ_2 and φ. These fibre's end regions, in fact, are far from the fibre exit point where the force is applied, so they are submitted to relatively low axial force, as can be seen by a small reacting force of the hooked part on the fibre (Fig. 8). As such, the energy absorption capacity in Fig. 10b showed a similar tendency of peak force. Moreover, lower internal angles ($\theta_2 = \varphi = 15^{o}$) lead to lower peak forces, due to the decreased resisting anchorage mechanisms necessary to extract the fibre from the channel.

3.4. *Effect of strength parameters (σ_u and f_{cm})*

Finally, the effects of fibre tensile strength σ_u and concrete compressive strength f_{cm} are investigated in Figs. 11 and 12. The analysis is carried out for fibres at 15^{o} and 60^{o} degrees, with a bond length $L_b = 30$ mm. All the other constitutive parameters are fixed according to the values in Eq. (6). The parameter K was obtained by using the empirical relationship $K = a\sqrt{f_{cm}}$, which was used to derive the pseudo "fibre's concrete foundation" from the concrete compressive strength. The coefficient a was determined by fitting the experimental data in Cunha et al. (2010), for which $K = 20$ GPa and the mean compressive strength of the concrete was 83.4 MPa.

The range of parameters σ_u and f_{cm} were chosen according to the strength of the steel fibres available in the market (500 MPa $\leq \sigma_u \leq$ 2500 GPa), and considering that, in the technology of FRC, f_{cm} ranges from 25 MPa up to 200 MPa. The results in Figs. 11 and 12 show that the concrete strength and the fibre tensile strength have both a significant influence on peak force and energy absorption capacity. In particular, both these indicators of the fibre reinforcement performance significantly increase with the concrete compressive strength. On the other hand, when fibre debonding is the main failure mode, an increase in the fibre tensile strength does not have any significant influence on the response, since the full fibre capacity is not reached.

4. Conclusions and future works

The pull-out behaviour of various configurations of a fibre reinforcement embedded in a concrete matrix was investigated by adapting the computational model recently proposed in Nonato Da Silva et al. (2019) to extend it for fibres with hooked end geometries. The fibre is modelled as a one-dimensional continuum for which axial, shear and bending internal work are accounted for. The interaction of the fibre with the concrete matrix is simulated by considering the fibre supported on a pseudo-foundation system, whose behaviour is modelled by cohesive-like constitutive laws for the orthogonal compressive pressure and for the sliding. The proposed approach is based on the solution of the system of differential equations that considers the equilibrium of forces, kinematics and constitutive laws of the intervenient materials. The additional complexities induced by the fibre misalignment were considered, including the transverse loading on the interface, bending of the fibre and the damage of the concrete matrix due to spalling.

A dimensional analysis gave physical insights into the model parameters that have the most influence on the pull-out response of the composite. Accordingly, a parametric analysis was carried out in terms of fibre embedment length, internal angles of the hook, and strengths of the fibre and of the concrete matrix. The results showed, and experimental results confirmed, that the pull-out response at a given fibre orientation is predominantly influenced by the mobilisation and straightening of the hook. Moreover, concrete compressive strength and fibre tensile strength predominantly affect the peak force, energy absorption capacity and failure mode.

With reference to the type of fibre used in Tarifa et al. (2020), two optimal configurations are found. One with $\theta_1 = 30^o$ and $L_b = 30$ mm, which maximises the peak force, and another with $\theta_1 = 15^o$ and $L_b = 30$ mm for which both peak force and energy absorption capacity are maximised. With respect to the 0° configuration tested by Tarifa et al. (2020), the analysis showed that a proper choice of the geometric parameters could lead to an increase of 34% in the peak force and 50% in energy absorption capacity. However, when the composite fails by fibre debonding, any increase in fibre strength does not contribute to ameliorate the composite response.

Future developments of this research include the optimization of the flexural response of an entire FRC beam failing in bending, by incorporating the proposed model in a numerical multiscale procedure such the one used in Nonato Da Silva et al. (2020). More complex geometries of the fibres can also be considered as the so-called 4D and 5D fibres, as well as the incorporation of viscous effects to account for the strain rate dependence observed during pull-out at different velocities.

Data availability

Data used in the present paper will be made available upon request.

Declaration of Competing Interest

The authors have no affiliation with any organization with a direct or indirect financial interest in the subject matter discussed in the manuscript.

Acknowledgments

The third and fourth authors wish to acknowledge the support by FEDER through the Operational Program for Competitiveness Factors - COMPETE and Internationalization Program (POCI), under the project NG_ TPfib POCI-01-0247-FEDER-033719.

References

Abrishambaf, A., Cunha, V.M., Barros, J.A., 2015. The influence of fibre orientation on the post-cracking tensile behaviour of steel fibre reinforced self-compacting concrete. Fract. Struct. Integr. J. 31 (31), 38–53.

Alessi, R., Ciambella, J., Paolone, A., 2017. Damage evolution and debonding in hybrid laminates with a cohesive interfacial law. Meccanica 52, 1079–1091. doi:10.1007/s11012-016-0437-8.

Alwan, J.M., Naaman, A.E., Guerrero, P., 1999. Effect of mechanical clamping on the pull-out response of hooked steel fibers embedded in cementitious matrices. Concr. Sci. Eng. 1 (1), 15–25.

Barros, J.A.O., Foster, S.J., 2018. An integrated approach for predicting the shear capacity of fibre reinforced concrete beams. Eng. Struct. J. 174, 346–357. doi:10.1016/j.engstruct.2018.07.071.

Cunha, V.M.C.F., Barros, J.A.O., Sena-Cruz, J.M., 2010. Pullout behavior of steel fibers in self-compacting concrete. J. Mater. Civil Eng. 22 (1), 1–9.

Fantilli, A.P., Vallini, P., 2007. A cohesive interface model for the pullout of inclined steel fibers in cementitious matrixes. J. Adv. Concr. Technol. 5 (2), 247–258.

Isla, F., Ruano, G., Luccioni, B., 2015. Analysis of steel fibers pull-out. experimental study. Construct. Build. Mater. 100, 183–193.

Khabaz, A., 2016. Monitoring of impact of hooked ends on mechanical behavior of steel fiber in concrete. Construct. Build. Mater. 113, 857–863.

Krenk, S., Høgsberg, J., 2013. Statics and Mechanics of Structures. Springer Netherlands, Dordrecht doi:10.1007/978-94-007-6113-1.

Lancioni, G., Alessi, R., 2020. Modeling micro-cracking and failure in short fiber-reinforced composites. J. Mech. Phys. Solids 137, 103854.

Laranjeira, F., Molins, C., Aguado, A., 2010. Predicting the pullout response of inclined hooked steel fibers. Cement Concr. Res. 40 (10), 1471–1487.

Mazaheripour, H., Barros, J.A.O., Sena-Cruz, J.M., 2016. Tension-stiffening model for FRC reinforced by hybrid FRP and steel bars. Compos. Part B: Eng. 88, 162–181.

Nonato Da Silva, C., Ciambella, J., Barros, J., Costa, I., 2019. Analytical bond model for general type of reinforcements of finite embedment length in cracked cement based materials. Int. J. Solids Struct. 167, 36–47. doi:10.1016/j.ijsolstr.2019.02.018.

Nonato Da Silva, C.A., Ciambella, J., Barros, J.A.O., dos Santos Valente, T.D., Costa, I.G., 2020. A multiscale model for optimizing the flexural capacity of FRC structural elements. Compos. Part B Eng. 200, 108325. doi:10.1016/j.compositesb.2020.108325.

Robins, P., Austin, S., Jones, P., 2002. Pull-out behaviour of hooked steel fibres. Mater. Struct. 35 (7), 434–442.

Soudki, K., Alkhrdaji, T., 2004. Guide for the Design and Construction of Externally Bonded FRP Systems for Strengthening Concrete Structures (ACI 440.2R-02) doi:10.1061/40753(171)159.

Soetens, T., Van Gysel, A., Matthys, S., Taerwe, L., 2013. A semi-analytical model to predict the pull-out behaviour of inclined hooked-end steel fibres. Construct. Build. Mater. 43, 253–265.

Song, F., 2012. Effect of fibre properties and embedment conditions on fibre pullout behaviour from concrete matrix H. S. Muller, M. Haist, and F. Acosta, 597602.

Tarifa, M., Poveda, E., Cunha, V.M.C.F., Barros, J.A.O., 2020. Effect of the displacement rate and inclination angle in steel fiber pullout tests. Int. J. Fract. 223, 109–122. doi:10.1007/s10704-019-00398-2.

Wang, Y., 1989. Mechanics of Fiber Reinforced Cementitious Composites. Massachusetts Institute of Technology.

Zhan, Y., Meschke, G., 2014. Analytical model for the pullout behavior of straight and hooked-end steel fibers. J. Eng. Mech. 140 (12), 91–104.

Zīle, E., Zīle, O., 2013. Effect of the fiber geometry on the pullout response of mechanically deformed steel fibers. Cement Concr. Res. 44, 18–24.